

Effect of step anisotropy on crystal growth inhibition by immobile impurity stoppers

James P. Lee-Thorp,^{*,†} Alexander G. Shtukenberg,^{*,‡} and Robert V. Kohn^{*,†}

[†]*Courant Institute of Mathematical Sciences, New York University, NY, USA*

[‡]*Department of Chemistry, New York University, NY, USA*

E-mail: leethorp@cims.nyu.edu; shtukenberg@mail.ru; kohn@cims.nyu.edu

Abstract

Step pinning by immobile stoppers is the most important crystal growth inhibition mechanism. It was first studied by Cabrera and Vermilyea in 1958, who considered the macroscopic effect of a periodic array of pinning sites. However, their analysis (and others since) involved uncontrolled approximations and did not consider what happens when step anisotropy induces faceting. Here we revisit the motion of a step past a periodic array of pinning sites, simulating the evolution numerically using a semi-implicit front-tracking scheme for anisotropic surface energies and kinetic coefficients. We also provide exact formulas for the average step velocity when the anisotropy is such that the interface is fully faceted. We compare the average step velocities obtained numerically to the estimates derived in the isotropic setting by Cabrera & Vermilyea (1958) and Potapenko (1993), and to the exact results obtained in the fully-faceted setting. Our results show that while the local geometry of the propagating step varies considerably with anisotropy, the average step velocity is surprisingly insensitive to anisotropy. The behavior starts changing only when the ratio between minimum and maximum values of the surface energy is roughly less than 0.1.

Introduction

Additives and impurities are major factors controlling the crystallization process. They can affect polymorphism and nucleation; change crystal morphology, composition, and crystallization kinetics; and modify crystal properties and perfections.¹⁻⁵ Revealing the mechanisms of crystal-additive interaction is one of the primary tasks of crystal growth science and is crucial for numerous practical applications. In this study, we consider the effect of additives on crystallization kinetics for crystals growing by step motion on flat surfaces. This includes most solution and vapor grown crystals as well as some melt grown crystals.

Additives can affect growth kinetics by shifting phase equilibria, changing solution speciation, and modifying solvation/desolvation energies and mobility of species.^{4,6} Stronger effects can be achieved if the additives compete with the growth units and decrease the number of active growth points as proposed in the Bliznakov-Chernov model.^{7,8} However, the strongest effect occurs when impurities and additives adsorb to the crystal surface, becoming stoppers that interfere with step propagation over the surface.

In 1958, Cabrera and Vermilyea considered the kinetics of step propagation past a periodic array of stoppers.⁹ They focused on strongly adsorbed stoppers on the crystal terrace, distributed over the surface in an idealized square grid (Figure 1). While the step is pinned by stoppers, it can advance in the region between them. When the spacing between the stoppers is small enough, the step is blocked by the “impurity fence” and comes to rest. When the spacing exceeds a critical value, however, the step gets past the stoppers by wrapping around them.

To make this picture quantitative, Cabrera and Vermilyea assumed as an approximation that although the curvature κ of the moving front varied with time, it was constant in space. As the step advances κ increases, the Gibbs-Thomson effect leads to a higher step free energy and, as a result, the step advancement slows down. If the stopper separation d is below the diameter of the critical nucleus, $2r_c$, the step cannot percolate through the array of stoppers and growth stops; this is the origin of the so-called “dead zone.” If, however, $\zeta = 2r_c/d < 1$,

then the step velocity reaches its minimum, $V_{\min} = V_0(1 - \zeta) > 0$, when $\kappa = 2/d$; at that moment the neighboring circular segments coalesce into a continuous step, thereby getting past the stoppers. The growth front becomes straight again, regaining its original velocity, V_0 , until it encounters the next line of stoppers. Cabrera and Vermilyea argued that the average step velocity V_{avg} is well-approximated by the geometric mean of the minimum step velocity and the velocity of the straight step; we shall refer to this as the C-V model:

$$V_{avg} = \sqrt{V_0 V_{\min}} = V_0 \sqrt{1 - \zeta}. \quad (1)$$

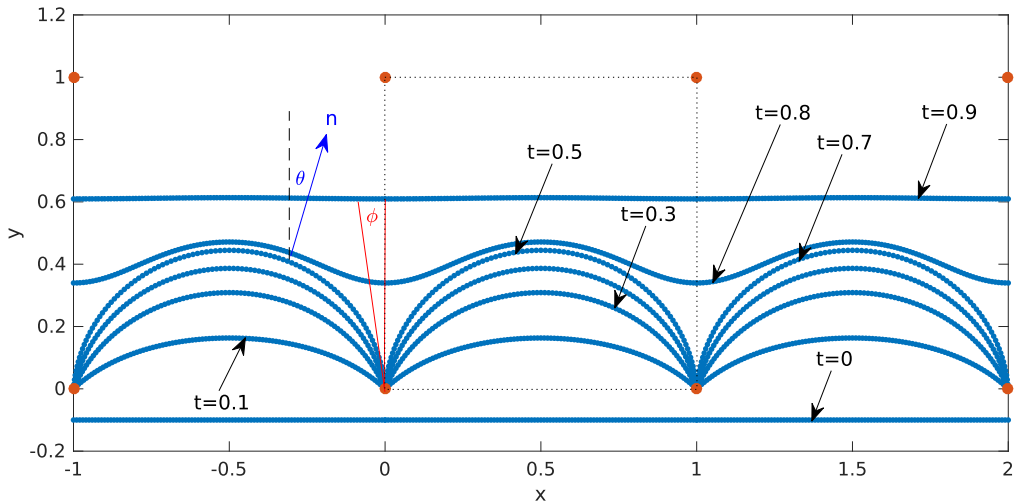


Figure 1: Propagation of an isotropic step through an array of immobile stoppers (orange dots) distributed over a square grid and separated by $d = 1$. The blue lines are fixed time snapshots. The step motion here corresponds to Eq. (5) with $M(\mathbf{n}) \equiv 1$, and $\gamma(\mathbf{n}) \equiv 1$. The angle θ (dark blue), defined at any point on the growth front, is the angle between the vertical direction and the normal \mathbf{n} to the front. The angle ϕ (red), defined at a stopper, denotes the “pinning angle”, which is the angle that the front makes with the vertical direction at the stopper.

Due to its simplicity and the clear physical meaning of all model parameters, the C-

V model has become a benchmark growth inhibition model. Indeed, the key features of the model – formation of a dead zone and roughening of the step edges – have been observed in many systems. However, direct comparison of Eq. (1) to experiment requires high quality kinetic measurements, which were not possible until atomic force microscopy and interferometric techniques were developed and applied to crystal growth problems. Today, such data are available for several systems, including potassium dihydrogen phosphate with Al^{3+} , Fe^{3+} and Cr^{3+} ,¹⁰ paracetamol with *p*-acetoxyacetanilide,¹¹ sodium chlorate with dithionate,¹² calcium oxalate monohydrate with citrate ion,^{13,14} calcium oxalate monohydrate with acidic peptides,^{15–18} calcite with Mg^{2+} and Sr^{2+} ,^{19–21} tetragonal lysozyme with proteins,^{22,23} and hexagonal L-cystine with L-cystine dimethylester and several other tailor-made additives,^{24,25} along with many other less precise measurements. None of these systems is perfectly described by the C-V model.

In particular cases some improvement has been achieved by playing with adsorption isotherms,^{13,14,26} taking into account a slow rate of adsorption,^{15,17,23,27–31} using a different expression for the driving force of crystallization,^{13,14} considering some fraction of the additive to block kinks in accordance with Bliznakov-Chernov model,^{13,14} using the arithmetic mean³² or minimum velocities^{13,14} instead of the geometric mean, or taking into account formation of macrosteps.^{33,34}

Potapenko modified the C-V model³⁵ by assuming that the step curvature increases from 0 to $1/r_c$, after which the step percolates through the impurity fence and its velocity becomes equal to V_0 . Also within this approximation he calculated the average velocity exactly rather than using a geometric mean estimate. This calculation gives the same percolation threshold as the C-V model, $\zeta = 2r_c/d = 1$, but it leads to a different expression for the average step velocity:

$$V_{avg} = V_0 \left(1 + \zeta \ln(1 - \zeta^2)/2 + \frac{\zeta^2}{\sqrt{1 - \zeta^2}} \operatorname{atan} \left(\frac{\zeta}{\sqrt{1 - \zeta^2}} \right) \right)^{-1}. \quad (2)$$

Eq. (2) sometimes works better than the C-V model (this occurs e.g. for potassium dihydrogen phosphate with trivalent metals¹⁰). However it still deviates significantly from

the actual kinetic behavior. This is not surprising given that both approaches make several approximations, including the assumption that step has constant curvature at each time.

There have been several numerical studies of crystal growth inhibition in recent years. Kinetic Monte-Carlo simulations have been used to study steps on the $\{001\}$ surface of a solid-on-solid (SOS) Kossel crystal for random and regular distributions of stoppers,^{36,37} different stopper sizes,^{36,37} different bond energies (the bond energy is related to step roughness and kink density),^{36,38–40} stoppers varying in their ability to be overgrown,³⁸ and stoppers varying in their mobility.³⁷ Ice crystallization in the presence of antifreeze proteins was simulated using molecular dynamics.⁴¹ Qualitatively, such simulations can capture many features of experimentally-observed kinetic curves. However, quantitative comparison is difficult as these simulations are stochastic by nature and mostly rely on specific models of the surface and associated intermolecular interactions. The consequences of spatial randomness and stopper size have also been explored using macroscopic phase-field simulations.⁴²

All previous studies considered isotropic surface energies. It is natural to ask to what degree such anisotropy influences the average step velocity. Lifting the assumption of a surface isotropy is very important because most crystal surfaces at low homological temperatures grow by polygonal steps and exhibit significant anisotropy. In fact, this is the case for all the examples cited in this paper except ice crystallizing in the presence of antifreeze proteins.²⁷ The propagation of steps in highly anisotropic systems is also important in other problems (unrelated to growth inhibition by impurities), for example in understanding how the velocity of a step depends on its length in the dislocation spiral growth mechanism.^{43–46}

The influence of growth anisotropy is the major focus of the present study, and we address it by simulating the step motion numerically using a semi-implicit front-tracking scheme. By performing numerical simulations with anisotropic surface energies and mobilities, we avoid the assumption of constant curvature and we take into account the presence of anisotropic step edge energies and kinetic coefficients, while keeping other physical assumptions behind the C-V model intact. Namely, we assume that: growth proceeds near equilibrium; the

kink mobility and density are high enough that the step velocity is determined pointwise by the Gibbs-Thomson law; the stoppers are immobile and large compared to the growth front fluctuations; the step cannot overgrow the stoppers directly; and the stoppers are distributed over a square grid (thus, the present study does not consider how things might be different when the impurity locations are random, and it does not permit the density of stoppers to change over time). We study growth inhibition from the macroscopic point of view by considering a step as a continuous line, setting aside the details of the kink structure. In our model the step motion is governed by a partial differential equation and the stoppers act as pinning sites; this excludes the possibility that fluctuations might help steps go past stoppers, and it does not consider impurities that merely slow rather than stop the step motion.

In choosing to do our simulations using a semi-implicit front-tracking scheme, we have made a selection. Other potential numerical approaches include (a) a fully-implicit rather than semi-implicit front tracking scheme; (b) a level-set method, i.e. one where the growth front at time t is represented as the zero-level-set of an evolving function of space and time; and (c) a phase-field method, i.e. one where the growth front is treated as a diffuse rather than sharp interface. For methods of type (a) and (b) applied to anisotropic front motion in the absence of stoppers see, for example, ref.⁴⁷; for a method of type (c) applied to isotropic front motion in the presence of stoppers see ref.⁴⁸. We have chosen a semi-implicit front-tracking scheme (similar to the approach of ref.⁴⁹) because it permits well-resolved and accurate simulations of our growth law (5). We did not attempt fully-implicit time-stepping as considered in⁴⁷ since the solution of its time-step problem requires a convex optimization; the main advantage of implicit time-stepping would be to permit adaptive time-stepping, a complication we found unnecessary. We did not use a phase-field or level-set method because these approaches require solving partial differential equations in two space dimensions rather than in one; as a result, simulations with the same spatial resolution as ours would require dramatically more computing time.

Simulations provide precise solutions to specific questions, but exact formulas provide a different type of insight. While closed-form solutions are not available for the motion laws we simulate, they are available in the closely-related setting of a fully-faceted growth front. It is natural to compare the numerical results for mostly-faceted growth fronts to the analytical results for full-faceted fronts. To facilitate this, we shall discuss some fully-faceted cases, obtaining formulas for the associated average step velocities.

We compare the average step velocities obtained numerically to the estimates derived in the isotropic setting by Cabrera & Vermilyea (1958) and Potapenko (1993), and to the exact solutions obtained in fully-faceted settings. In aggregate, we demonstrate that while the local geometry of the propagating step varies considerably with anisotropy, the overall growth rate is surprisingly insensitive to mild anisotropies that include almost all realistic examples of faceted steps. The effect of anisotropy becomes significant only if the ratio between the minimum and maximum surface energies $\gamma_{\min}/\gamma_{\max} \lesssim 0.1$, which is not typical for most crystals.

Modeling

Step motion law

The normal velocity of a straight step, V_0 , can be expressed as the product of the driving force for crystallization, usually expressed as a difference in chemical potentials between the bulk of the crystal and growth medium, $\Delta\mu$, and a proportionality factor β called the kinetic coefficient: $V_0 = \beta\Delta\mu$. For a curved isotropic step, this law should be corrected by a term $\delta\mu_\kappa = \omega\gamma/r$ associated with the decrease of the driving force for crystallization due to the step curvature $\kappa = 1/r$, where γ is the surface energy and ω is the molar volume:

$$V = \beta(\Delta\mu - \delta\mu_\kappa) = V_0(1 - \omega\gamma\kappa/\Delta\mu). \quad (3)$$

For an anisotropic macroscopic model of step motion, one can write down a similar law, in which the normal step velocity is given by a geometric equation of the form

$$V = M(\mathbf{n})(\sigma - \xi\kappa_\gamma(\mathbf{n})). \quad (4)$$

Here, the difference in chemical potentials, $\Delta\mu$, is expressed through dimensionless supersaturation σ . The role of the kinetic coefficient is played by an orientation dependent mobility factor, $M(\mathbf{n})$, and the surface energy correction is described through the weighted mean curvature, $\kappa_\gamma(\mathbf{n})$ ⁵⁰; here \mathbf{n} denotes the vector normal to the front, and $0 \leq \xi \leq \xi_c$ is a percolation parameter. If ξ becomes equal to ξ_c , then the driving force for crystallization is equal to the curvature related increase in the surface energy, $\sigma = \xi_c\kappa_\gamma(\mathbf{n})$, and the normal velocity is zero: $V = 0$. Alternatively, one can define the critical supersaturation, at which $V = 0$, as $\sigma_c = \xi\kappa_\gamma(\mathbf{n})$. In terms of the standard C-V formulation (Eq. (1)), we have that $\zeta = \xi/\xi_c = \sigma_c/\sigma = 2r_c/d$.

For numerical simulation, it is convenient to non-dimensionalize the geometric growth law (4). Recall that the normal velocity of a straight step (no curvature) is given by V_0 , that the distance between the stoppers is d , and that the supersaturation, σ , is dimensionless. Rescaling space by $\mathbf{x} = (d)\tilde{\mathbf{x}}$ and time by $t = (d/V_0\sigma)\tilde{t}$, we can rewrite (4) as

$$\tilde{V} = \tilde{M}(\mathbf{n})(1 - \tilde{\xi}\tilde{\kappa}_\gamma(\mathbf{n})), \quad (5)$$

where \tilde{V} , $\tilde{M}(\mathbf{n}) \equiv M(\mathbf{n})/V_0$, $\tilde{\xi} \equiv \xi/(\sigma d)$ and $\tilde{\kappa}_\gamma(\mathbf{n})$ are, respectively, the dimensionless normal velocity, mobility, percolation parameter, and weighted mean curvature. In the remainder of this paper, we will numerically simulate and analyze the non-dimensional law (5), but always plot and present our results in terms of the dimensional parameters: V , ξ and σ . Where convenient in the text, we will drop the tilde superscripts that appear in Eq. (5).

Stoppers

In experiments, the location of impurity stoppers is more or less random. However, a natural first step is to study the influence of stoppers in a more controlled geometry such as the periodic square grid used by Cabrera and Vermilyea⁹, where one can get a quantitative and qualitative understanding of their effects. If the impurity concentration is low, the step will eventually close around and incorporate the stoppers into its bulk. This scenario is illustrated in Figure 1. The step approaches an impurity fence (orange dots) and is initially pinned at several sites. As the front continues to advance away from a particular stopper, the “pinning angle”, ϕ , decreases. When $\phi \approx 0$, the front will close around the impurity and continue to advance unimpeded. Exactly what we mean by “ $\phi \approx 0$ ”, i.e. how we define our pinning angle breakthrough threshold, is an important modeling decision which we discuss when we present our numerical results. If, on the other hand, the impurity concentration is sufficiently high, then the pinning angle will remain nonzero and above the breakthrough threshold, and the front will become completely pinned by the impurity fence.

The preceding discussion applies to our numerical simulations. For fully-faceted interfaces, the treatment of breakthrough must be different; this is discussed below, when we discuss the analytical solution formula in the fully-faceted setting.

Anisotropic surface energies

In considering anisotropic surface energies, we are mainly interested in how the presence of facets influences interactions of moving steps with impurities. Therefore we focus on examples where faceting occurs: our numerical studies involve surface energies of the form

$$\gamma(\theta) = \frac{1 + c_1 |\sin(\theta)| + c_2 |\sin(2\theta)| + c_3 |\sin(3\theta)|}{1 + c_1 + c_2 + c_3}, \quad (6)$$

where the constants c_1 , c_2 , and c_3 satisfy

$$c_1, c_2, c_3 \geq 0, \quad c_2 < 1/3, \quad \text{and} \quad c_3 < 1/8. \quad (7)$$

The upper limits imposed on c_2 and c_3 correspond to the maximal anisotropy at which the Frank diagram remains convex ($\gamma(\theta) + \gamma''(\theta) > 0$, see below). When at least one of the c_j is positive, this γ is not smooth; for numerical simulation we use a regularized version:

$$\gamma_\epsilon(\theta) = \frac{1 + c_1\sqrt{\sin^2(\theta) + \epsilon^2} + c_2\sqrt{\sin^2(2\theta) + \epsilon^2} + c_3\sqrt{\sin^2(3\theta) + \epsilon^2}}{1 + c_1 + c_2 + c_3}, \quad (8)$$

where ϵ is small but positive. The dependence of our numerical results upon ϵ is considered in the Supporting Information. A physical justification for the regularization is discussed later in this section.

The evolution associated with a surface energy of the form Eq. (6) does not have closed-form solutions. There is, however, a class of anisotropic examples where the evolutions do have closed-form solutions; this occurs in the *fully-faceted* case, when the Frank diagram of γ is a polygon. It is natural to compare the numerical solutions obtained using Eq. (6) with the analytical results for analogous fully-faceted examples. Therefore, besides anisotropies of the form (6), we also consider a corresponding family of fully-faceted examples.

Before discussing our examples in more detail, we briefly review some well-known facts about anisotropic surface energies for curves in the plane (see e.g. refs. ^{49–51}):

- (a) For any surface energy $\gamma(\theta)$ it is useful to consider its *Frank diagram* and its *Wulff shape*.

The Frank diagram is the polar plot of $1/\gamma$; the Wulff shape is $\{x : x \cdot \mathbf{n}_\theta \leq \gamma(\theta)\}$, where $\mathbf{n}_\theta = (\sin \theta, \cos \theta)$ is the unit vector in direction θ ; see Figure 1.

- (b) The *weighted mean curvature* κ_γ is the first variation of the surface energy; in other words, for a moving curve $\Gamma(t)$, $\frac{d}{dt} \int_{\Gamma(t)} \gamma(\theta(s)) ds = \int_{\Gamma(t)} V(s) \kappa_\gamma(s) ds$. Here s represents arc length along the moving curve, $\theta(s)$ is the angle of the normal direction, and V

is the normal velocity of the moving curve. For a smooth surface energy, κ_γ has the simple expression $\kappa_\gamma(s) = (\gamma(\theta(s)) + \gamma''(\theta(s))) \kappa(s)$ where κ is the geometric curvature of the curve at position s .

(c) The Frank diagram helps one see the well-posedness of the evolution law (4). Indeed, for smooth surface energies the evolution is well-posed – reducing to a nonlinear parabolic differential equation – when $\gamma(\theta) + \gamma''(\theta) \geq 0$, and this is equivalent to the Frank diagram being convex.

(d) The Frank diagram also helps one see the presence or absence of facets. Indeed: if the Frank diagram of γ has a convex corner at $\theta = \theta_0$, then a curve evolving according to Eq. (4) has a facet at orientation θ_0 . Similarly, if the Frank diagram has a slightly rounded corner (as occurs for our regularized surface energy in Eq. (8)) then the evolving curve has an approximate facet. To see why, note that the weighted mean curvature $\kappa_\gamma = (\gamma + \gamma'')\kappa$ should stay bounded (since the normal velocity is bounded); since $\gamma + \gamma''$ is very large near θ_0 , it follows that the geometric curvature κ must be very small near θ_0 . When the Frank diagram has a sharp corner at θ_0 , the weighted mean curvature becomes nonlocal: its value on a facet with normal angle θ_0 takes the constant value

$$\kappa_\gamma = \frac{\text{jump in } \gamma' \text{ at } \theta_0}{\text{length of the facet}} \equiv \frac{[\gamma'(\theta_0)]}{L}. \quad (9)$$

To explain (somewhat heuristically), we observe that

$$\int_{\text{facet}} V (\gamma(\theta(s)) + \gamma''(\theta(s))) \kappa ds = \int_{\text{facet}} V \frac{d}{ds} \gamma'(\theta(s)) ds$$

(the term $\gamma(\theta(s))\kappa$ on the left vanishes since $\kappa = 0$ on the facet; the $\gamma''(\theta(s))\kappa$ term has been rewritten using definition of geometric curvature, $\kappa = d\theta/ds$). Since the normal velocity V must be constant on a facet, the last expression is simply the product of the velocity V times the jump in γ' . This in turn equals $\int_{\text{facet}} V \kappa_\gamma ds$ when κ_γ is given

by Eq. (9).

- (e) The Wulff shape solves the anisotropic isoperimetric problem, i.e. it minimizes surface energy for given volume. As a consequence, the Wulff shape has the property that κ_γ is constant along its boundary. The relevance to our motion law $V = M(\mathbf{n})(\sigma - \xi\kappa_\gamma(\mathbf{n}))$ is this: if the interface is pinned by the stoppers (i.e. if $\xi \geq \xi_c$), then the pinned configuration solves $\sigma - \xi\kappa_\gamma = 0$, i.e. it is a piece of a Wulff shape.

Turning now to the specific family of anisotropic surface energies given by Eq. (6), we begin by recalling the significance of the restrictions imposed by Eq. (7) upon the constants c_j : they assure that $\gamma + \gamma'' \geq 0$, so that the Frank diagram is convex and the evolution law (4) is well-posed.

When $c_1 > 0$ but $c_2 = c_3 = 0$, the Frank diagram is a lens-shaped body (Figure 2 second column, bottom row). We call these examples *single-facet* surface energies. Actually there are two faceting directions ($\theta = 0, \pi$); however due to the symmetry of our problem, the normal angles of our evolving curves are restricted to $-\pi/2 < \theta < \pi/2$, so only one one faceting direction will be seen: $\theta = 0$ (normal to the overall growth direction). As c_1 increases, the angle in the Frank diagram gets sharper (Figure 3, top row); in practice this makes the facet at $\theta = 0$ more prominent. The Wulff shape for this class of surface energies is a “stadium” – its boundary consists of two facets and two semicircles; as c_1 increases the facets get longer. Since we divide by $1 + c_1 + c_2 + c_3$ in Eq. (6), taking c_1 large makes the surface energy very anisotropic and the faceting prominent, but it has relatively little effect on the overall magnitude of the surface energy. In fact, one can show that when $c_2 = c_3 = 0$, the value of ξ_c is independent of c_1 .

When $c_3 > 0$ but $c_1 = c_2 = 0$ the Frank diagram varies from a circle (when $c_3 = 0$) to a shape closely resembling a regular hexagon as c_3 approaches $1/8$ (Figure 2 final column, bottom row). We call these examples *symmetric triple-facet* surface energies, because there are three symmetry-related facets ($\theta = -\pi/3, 0$, and $\pi/3$) in the relevant interval $|\theta| < \pi/2$.

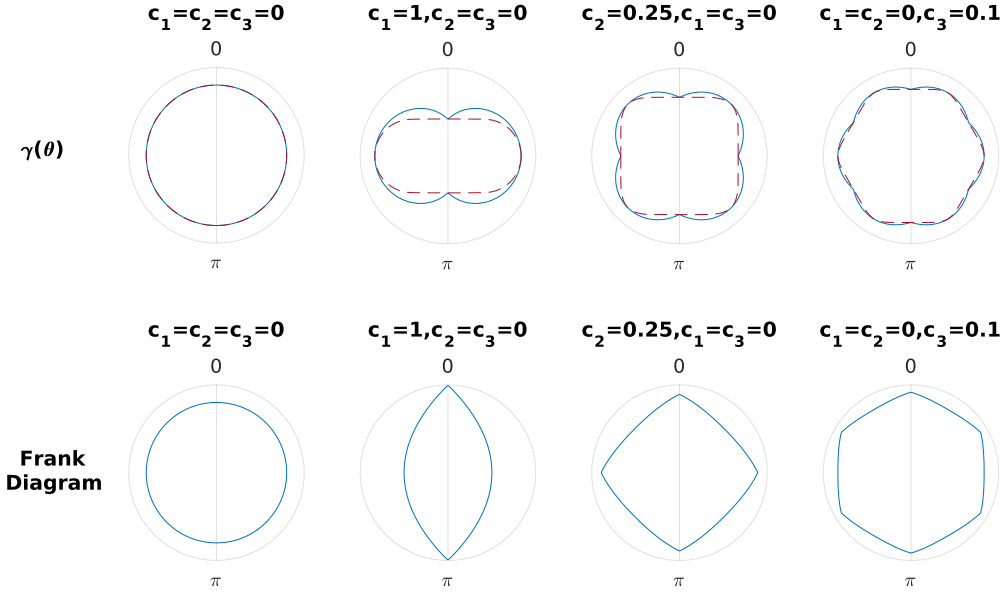


Figure 2: Polar plots of the surface energy $\gamma(\theta)$ (**top row**) and the corresponding Frank diagrams (polar plots of $1/\gamma$) (**bottom row**). Wulff shapes are shown in red (dashed lines). Each plot title displays the corresponding c_1 , c_2 and c_3 values in Eq. (6). $\mathbf{c}_1 = \mathbf{c}_2 = \mathbf{c}_3 = \mathbf{0}$: Isotropic surface energy. The corresponding step motion is shown in Figure 4 (leftmost column). The Wulff shape and the surface energy match in the isotropic case. $\mathbf{c}_1 = \mathbf{1}, \mathbf{c}_2 = \mathbf{c}_3 = \mathbf{0}$: The surface energy has a corner (γ' is discontinuous) at $\theta = 0$ (and $\theta = \pi$). The step motion therefore exhibits a single facet in the vertical direction; see Figure 4 (second column). $\mathbf{c}_2 = \mathbf{0.25}, \mathbf{c}_1 = \mathbf{c}_3 = \mathbf{0}$: The surface energy has corners at $\theta = n\pi/2$, for $n = 0, 1, 2, 3$, leading to double-faceted growth; see Figure 4 (third column). $\mathbf{c}_3 = \mathbf{0.1}, \mathbf{c}_1 = \mathbf{c}_2 = \mathbf{0}$: The surface energy has corners at $\theta = n\pi/3$, for $n = 0, 1, \dots, 5$, leading to triple-faceted growth; see Figure 4 (rightmost column).

Note that while the facets are symmetry-related from the perspective of surface energy, $\theta = 0$ is still distinguished by being normal to the overall growth direction.

We can interpolate between the single-facet case and the symmetric triple-facet case by taking both c_1 and c_3 positive (while keeping $c_2 = 0$). For example, holding $c_3 = 1/10$ and increasing c_1 we get a family of *triple-facet* surface energies that interpolate between the symmetric triple-facet case (when c_1 is near 0) and the single-facet case (when c_1 is large); see Figure 3, bottom row. The Wulff shapes for these examples have facets separated by smooth curves – one can view them as polygons with rounded corners. When c_1 is large, the polygon is a six-sided approximation of a long, thin stadium.

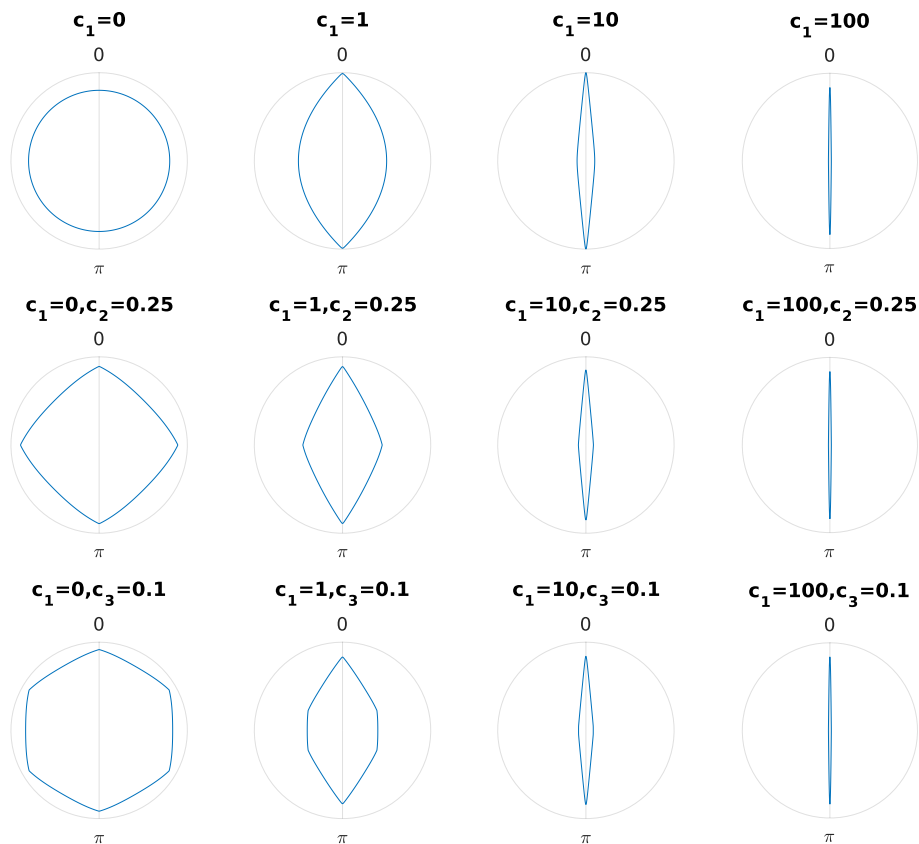


Figure 3: Frank diagrams for single-, double- and triple-facet surface energies. **Top row:** $c_1 \neq 0$ and $c_2 = c_3 = 0$. **Middle row:** $c_2 = 0.25$, $c_1 \neq 0$, and $c_3 = 0$. **Bottom row:** $c_3 = 0.1$, $c_1 \neq 0$, and $c_2 = 0$. As c_1 increases, the Frank diagram becomes increasingly elongated and the facet length increases.

Our triple-facet examples have $c_2 = 0$ and $c_3 > 0$. The opposite choice $c_2 > 0$, $c_3 = 0$ gives

an analogous family of *double-facet* surface energies. When $c_1 = c_3 = 0$ we get symmetric double-facet examples (Figure 2 third column, bottom row), whose Frank diagrams vary from a circle (when $c_2 = 0$) to a shape closely resembling a square as c_2 approaches $1/3$. By increasing c_1 while holding, for example, $c_2 = 1/4$, we get a family of double-facet surface energies that interpolate between the symmetric double-facet case and the single-facet case; see Figure 3, middle row. The Wulff shapes for this class of examples are rectangles with rounded corners.

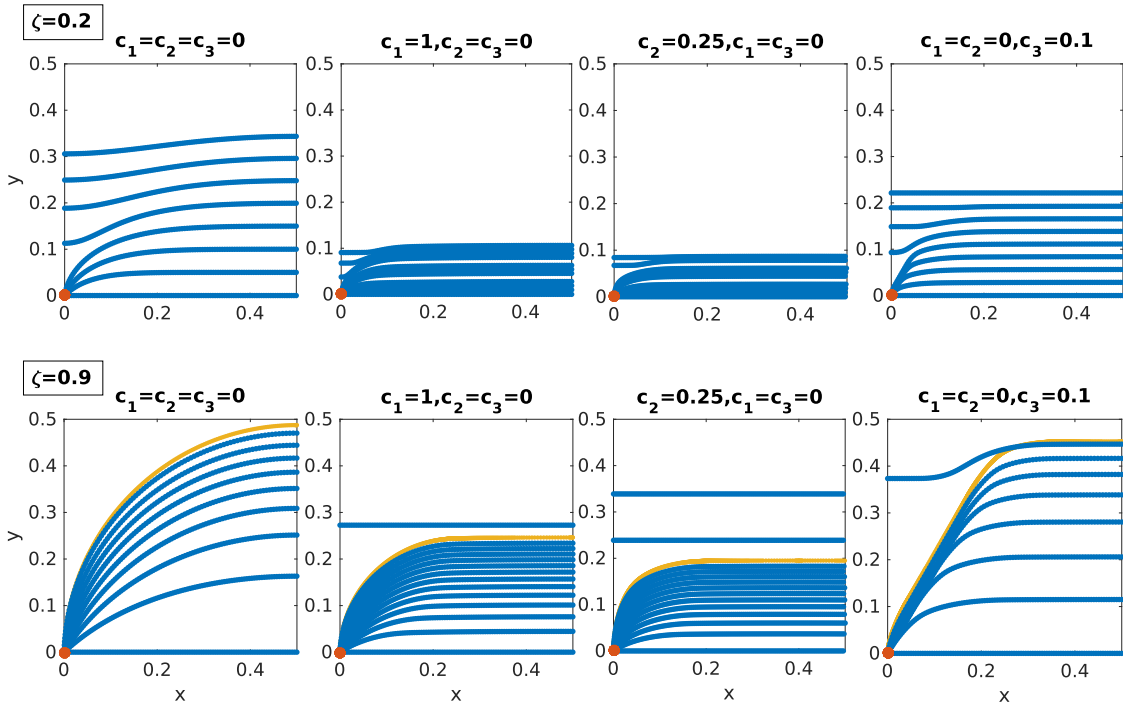


Figure 4: Fixed time snapshots of front evolution for the growth law (5) with $M(\mathbf{n}) \equiv 1$ and $\gamma(\mathbf{n})$ given by the corresponding panel in the top row of Figure 2. Only the left half of the fronts in a single period cell are shown; the right half may be inferred by symmetry. **Top row:** $\zeta \equiv \xi/\xi_c = 0.2$ – far from the pinning limit. **Bottom row:** $\zeta \equiv \xi/\xi_c = 0.9$ – near the pinning limit. Yellow curves denote stationary front configurations corresponding to $\zeta = 1$ ($\xi = \xi_c$).

How does anisotropy affect the actual geometry of the growth front? The answer is encapsulated by Figure 4. For the symmetric triple-facet surface energy (with c_3 large enough that faceting is prominent), when the front is attached to the stoppers it consists of facets connected by short curved regions (rightmost column of the Figure 4). For the

single-facet surface energy (with c_1 large enough that faceting is prominent), the only facet is at $\theta = 0$, so there is a large curved region near the stopper (second column of the Figure 4). The solution with our double-facet surface energy (third column of the Figure 4) is very similar to that for the single-facet surface energy, since our numerical pinning angle threshold is always positive (so θ is bounded away from $\pm\pi/2$ and vertical facets never form).

We turn now to the question why it is natural to consider surface energies of the form (6). The answer is that for this class of examples the anisotropy is strong enough for the moving interface to have facets, but mild enough that the Frank diagram remains strictly convex. This is important: if the Frank diagram were nonconvex then the motion law would be ill-posed, and a planar front whose normal angle satisfied $\gamma(\theta) + \gamma''(\theta) < 0$ would be unstable. There are, to be sure, material systems whose (zero-temperature) surface energies have nonconvex Frank diagrams. For such systems the analogue of the interface motion law (4) is obtained by convexifying the Frank diagram and using the associated convex (but not strictly convex) γ . Convexification of the Frank diagram corresponds physically to replacing a straight but unstable curve by a fine-scale mixture of different orientations with the same average slope. Our hypothesis that $\gamma + \gamma''$ is strictly positive reflects our desire to avoid systems where such behavior occurs. As justification, we note that convexification of the Frank diagram is a zero-temperature calculation. However, crystal growth occurs at finite temperature, and it is mediated by the formation and motion of kinks (as noted earlier, we consider a step with a high kink density). The thermal roughness induced by the presence of kinks should make the macroscopic surface energy strictly convex rather than degenerate-convex (i.e. it should make $\gamma + \gamma'' > 0$). This view is confirmed by physical observations of many systems, which reveal that corners between straight step segments are always rounded even when faceting occurs.^{43,44}

Our discussion has mainly focused on the nonsmooth surface energies given by Eq. (6). In practice, as already noted, our simulations use the regularized approximation (8). This amounts to rounding the corners of the Frank diagram. Besides being convenient numerically,

the use of a regularized γ is also quite plausible physically. Indeed, the thermal roughness associated with the presence of kinks should have some smoothing effect on the macroscopic surface energy.

As we have just explained, for real crystals growing at finite temperature the Frank diagram of the surface energy should be strictly convex with slightly rounded corners. This rules out the fully-faceted case, when the Frank diagram is a convex polygon. But we expect that the behavior of a mostly-faceted case and a corresponding fully-faceted case should be similar. This is useful, since we can solve the fully-faceted case analytically, thereby obtaining an approximate solution for the mostly-faceted case. Thus, besides considering surface energies of the form (6) we will also consider some cases where the Frank diagram is a polygon and the motion is fully-faceted. (By comparing the numerical and analytical results, we shall confirm that both models capture the behavior seen when the anisotropy is prominent enough to make the Frank diagram approximately polygonal.)

Numerical methods

Front tracking is a natural numerical scheme for evolving 1D curves in the plane. The basic algorithm consists of discretizing the front (a 1D curve), and evolving each point along the curve according to the normal velocity law (5). Because the impurities are distributed in a periodic lattice in our model problem, it suffices to consider a single period cell (the dotted square in Figure 1). We pin the ends of the curve at the impurity sites until the pinning angle, ϕ , falls below the pinning angle breakthrough threshold, ϕ_c . Once the front breaks through the impurity barrier, we evolve the curve with periodic boundary conditions.

We need to contend with a two numerical subtleties. First, anisotropies of the form shown in Eq. (6) introduce numerical stiffness into our problem, which we deal with using a semi-implicit scheme. Second, as the front evolves, we reparameterize the points along the curve to ensure that they remain equidistantly spaced. This avoids losing accuracy in some regions due to inadequate resolution.

For further details about our numerical methods, see the Supporting Information.

Analytical solution for fully-faceted cases

In many experimental systems, 2D nuclei and dislocation spirals on the crystal face have polygonal shapes with a minimal development of curved segments between them. This means that the surface energy anisotropy is significant and the Frank diagram and Wulff shapes are approximately polygonal. We may suppose, as a model, that curved segments are completely absent and the Frank diagram and Wulff shapes are exactly polygonal. The advantage of such a model is the availability of exact solution formulas. We expect (and our results show) that this approach can provide a good description of the real behavior of crystals with approximately polygonal Wulff shapes.

Lest there be any confusion, we emphasize that a surface energy with polygonal Wulff shape and Frank diagram cannot be represented in the form (6). However, given the facet orientations θ_i and the associated values $\gamma(\theta_i)$, it is easy to get a formula for γ when the Frank diagram is a polygon, by using the fact that $\gamma''(\theta) + \gamma(\theta) = 0$ at all angles other than the facet orientations.

Using Eq. (9), the weighted mean curvature of a straight step with orientation θ_0 can be computed from the step length, L , and the jump in the surface energy $[\gamma'(\theta_0)]$. For the setup in Figure 5, where the middle straight facet (with orientation θ_0) is located between two other straight facets (with orientations θ_+ and θ_- , respectively), the jump in surface energy is determined by the surface energies and orientations of the two neighboring facets. Using that $\gamma''(\theta) + \gamma(\theta) = 0$ on a facet, one can show^{49,51} that the jump is given by

$$[\gamma'(\theta_0)] = \gamma(\theta_-) \csc(\theta_0 - \theta_-) + \gamma(\theta_+) \csc(\theta_+ - \theta_0) - \gamma(\theta_0)(\cot(\theta_0 - \theta_-) + \cot(\theta_+ - \theta_0)). \quad (10)$$

The step velocity can be obtained from Eqs. (4), (9), and (10) for each step orientation. Combining all the constants into a single constant, called the critical length L_c , we obtain

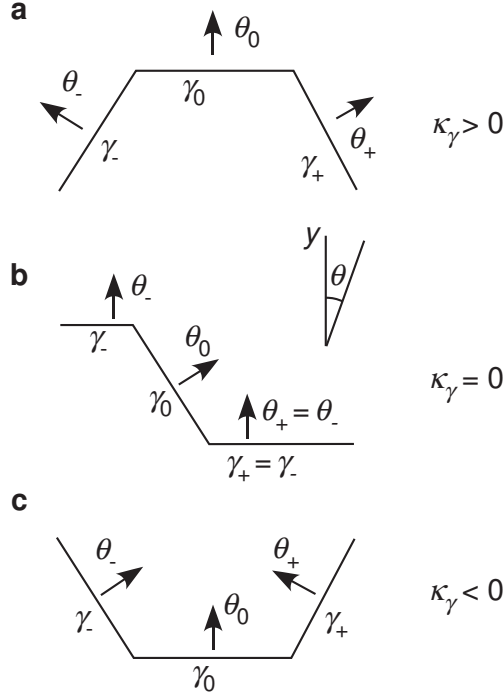


Figure 5: Illustration of application of Eq. (10). θ is the angle between the normal to the facet and vertical direction.

the well known growth law:⁴⁶

$$V = V_0 \left(1 - \frac{L_c}{L} \right). \quad (11)$$

The fact that the velocity of a facet depends linearly on $1/L$ (where L is the facet length) is confirmed by our numerical simulations in the Supporting Information (Figure S.4). For the formation of a 2D nucleus or a dislocation spiral, the critical length, L_c , is always positive, and the step does not move if $L < L_c$. For the other configurations shown in Figure 5, L_c can be zero or negative.

Since we are interested in the effect of stoppers, we must specify the circumstances under which the growth front breaks through the impurity fence. In the full-faceted setting, breakthrough occurs when two parts of the front (on either side of the stopper) overlap. For the fully-faceted analogue of our triple-facet case, this occurs when the facets with orientations $\theta = \pm\pi/3$ reach their critical length L_c ; see Figure S.3 in the Supporting Information. For the fully-faceted analogue of our double-facet case, breakthrough occurs when the facets

with orientations $\theta = \pm\pi/2$ reach their critical length L_c ; see Figure S.2 in the Supporting Information. This model for breakthrough is open to criticism in the double-facet case, since it permits vertical facets to form on both sides of the stopper without breakthrough.

As in Figure 5, let θ_0 , θ_- and θ_+ denote the orientations of the top, left neighboring and right neighboring facets. Denote by L_{c0} , L_{c-} and L_{c+} the critical lengths associated with each of these respective facets. Let $\theta_0 = 0$ be the growth direction. Our breakthrough criterion says that the step can percolate through the impurity fence if the distance between stoppers, d , exceeds a certain length. For the symmetric case where the surface energy is equal in left and right facet directions ($\gamma_- = \gamma_+$), the percolation parameter, $0 \leq \zeta \leq 1$, can be introduced as

$$\zeta = \frac{2L_{c-} \cos \theta_- + L_{c0}}{d} \quad (12)$$

During its propagation between two rows of stoppers, the fully-faceted step undergoes several configurational changes. The stages are illustrated in Figures S.2 and S.3 in the Supporting Information. In first stage, the horizontal segment moves with velocity given by Eq. (11), where $L_c = L_{c0}$. The size of the facet will change if its neighboring facets are not perpendicular to the growth front. However, the neighboring facets cannot move until their lengths exceed their corresponding critical values, L_{c-} and L_{c+} . During the second stage, the side facets move with velocity V_0 . Once the side facets begin to move, the stoppers immediately get incorporated and do not affect the step propagation anymore. At the point of junction where the side facets meet, two side facets form a new horizontal facet. This new horizontal facet propagates with velocity Eq. (11), where $L_c = -L_{c0}$. Since the bottom facet moves faster than the top one, they eventually merge restoring a straight growth front. The third stage corresponds to growth of a straight step with V_0 until the vertical coordinate of the step becomes $y = d$. The average step velocity can be calculated from times τ_1 , τ_2 , and τ_3 needed for the step to complete each of these three stages:

$$V_{avg} = \frac{d}{\tau_1 + \tau_2 + \tau_3}. \quad (13)$$

We have obtained analytical expressions for V_{avg} in the double- and triple-facet cases. Details of the calculations are given in the Supporting Information; here we simply report the results. Denote by L_{cs} and L_{ch} , the critical lengths for the vertical/side and horizontal facets, respectively. For the double-facet case, the percolation parameter is found using Eq. (10) to be $\zeta = L_{ch}/d$. The average step velocity is

$$V_{avg} = V_0 \frac{1 - \zeta}{1 - \zeta + \alpha \zeta^2}, \quad (14)$$

where $\alpha = L_{cs}/L_{ch}$ is the ratio between the critical lengths for the vertical/side and horizontal facets. Recalling that $L_c \propto \kappa_\gamma$ and using Eqs. (10) and (11), one sees that this parameter also characterizes the anisotropy of the surface energy: $\alpha = \gamma_h/\gamma_s$.

For the triple-faceted case, the percolation parameter turns out to be $\zeta = (L_{ch} + L_{cs})/d$, and $\alpha = L_{cs}/L_{ch} = \gamma_h/(2\gamma_s - \gamma_h)$. The average step velocity is given by

$$V_{avg} = V_0 \left(1 + \frac{\sqrt{3}}{2} \frac{\zeta}{1 + \alpha} \ln \left(\frac{e^\alpha(1 + \alpha - \zeta)}{(e^\alpha(1 + \alpha + \zeta(1 - \alpha)) - \zeta)(1 - \zeta)} \right) \right)^{-1}. \quad (15)$$

Results and discussion

Numerically, we compute the average velocity of the evolving front as follows. For a fixed ξ and lattice size, we evolve Eq. (5) in a periodic lattice of impurities until a dynamical (time periodic) steady state is reached. The steady state is reached when, within numerical resolution: (a) the front has the same configuration each time it hits consecutive impurity fences (rows of impurities) and (b) the front takes the same amount of time to move from one impurity fence to the next. The average velocity, V_{avg} , is then calculated from the time that elapsed in (b).

Isotropic surface energy

Figure 6a shows the average velocity of the evolving front as a function of the percolation parameter, ξ , for isotropic surface energy ($c_1 = c_2 = c_3 = 0$ in Eq. (6)), and constant mobility, $M(\mathbf{n}) = 1$. In experiment, this type of plot corresponds to dependence of step velocity on the distance between adsorbed impurities (for the Henry's isotherm, square root of the impurity concentration in the growth medium) at constant supersaturation. Results for three different pinning angle thresholds, ϕ_c (see Figure 6), indicate only a slight sensitivity of the numerical solution on the value of ϕ_c . Figure 6b plots the average velocity as a function of the supersaturation, σ , for the growth law (4). For $\sigma \gg \sigma_c$, the effect of stoppers becomes negligible and the average velocity approaches the asymptote $V_{avg} = V_0 = \sigma$. In experiment, plots such as Figure 6b characterize the effect of supersaturation for constant impurity concentration.

Compared to the numerical results, the C-V formula⁹ is generally inaccurate, even in the near pinning limit. The Potapenko prediction,³⁵ on the other hand, closely matches the numerical results near the pinning limit. Far from the pinning limit, $\xi \ll \xi_c$, both predictions fail because the front is not well approximated by arcs of circles; the C-V formula underestimates the velocity whereas Potapenko's formula overestimates the velocity. A similar conclusion was previously reached by Miura⁴² based on phase-field modeling of step percolation through an array of large stoppers.

Low anisotropy of surface energy

We begin our analysis of the influence of surface anisotropy by considering relatively mild anisotropies, i.e. those for which the ratio $\gamma_{\min}/\gamma_{\max}$ is close to 1. This case is important because it includes the common situation in which the Wulff shape is roughly polygonal with moderate eccentricity. Examples include our symmetric double-facet example (given by Eq. (6) with $c_1 = c_3 = 0$ and c_2 near its maximum value $1/3$, for which $\gamma_{\min}/\gamma_{\max} = 3/4$), and the analogous fully-faceted case when the Wulff shape is a square. Another example is our

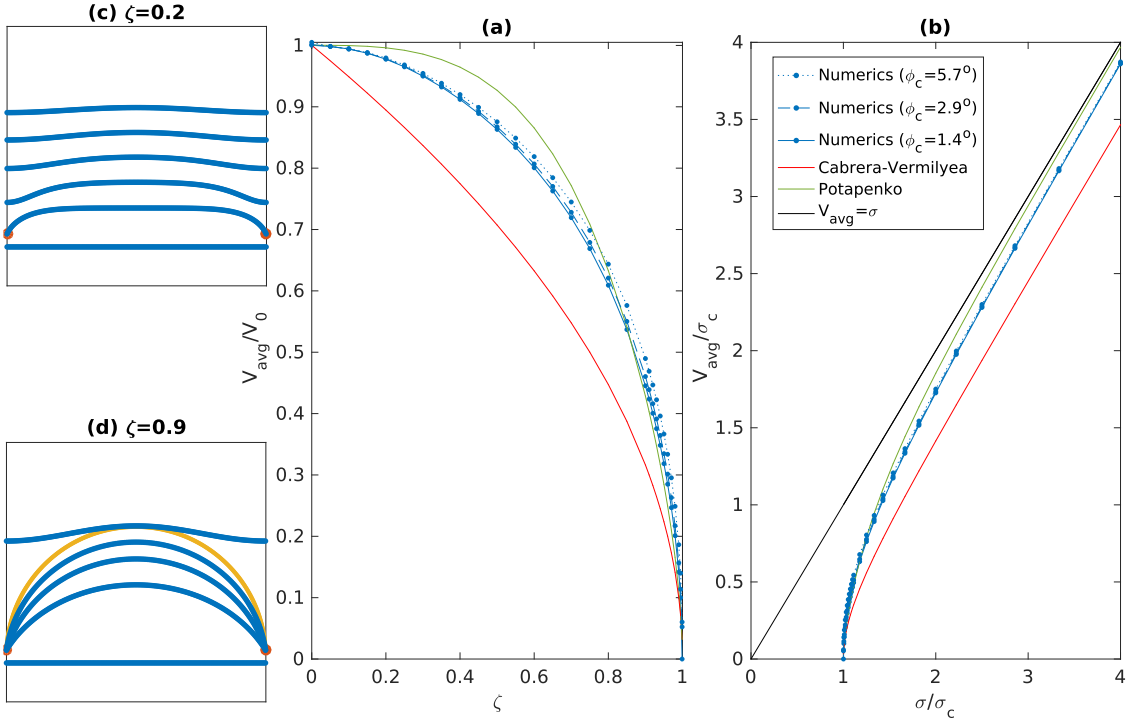


Figure 6: Average step velocity as a function of **(a)** the percolation parameter $\zeta = \xi/\xi_c$ and **(b)** the supersaturation σ/σ_c for isotropic surface energy and mobility. Results of simulations are shown for three different pinning angle thresholds, ϕ_c . The C-V and Potapenko predictions are shown in red and green, respectively. Panels **(c)** and **(d)** illustrate a series of fixed time front snapshots for $\zeta = 0.2$ and $\zeta = 0.9$, respectively ($\phi_c = 2.9^\circ$). The yellow curve in (d) is the stationary front configuration, corresponding to $\zeta = 1$.

symmetric triple-facet case (given by Eq. (6) with $c_1 = c_2 = 0$ and c_3 near its maximum value $1/8$, for which $\gamma_{\min}/\gamma_{\max} = 8/9$), and the analogous fully-faceted case when the Wulff shape is a regular hexagon. Simulations for these cases are shown in Figure 7 along with simulations for the isotropic case and for a single-facet case with mild anisotropy, $c_2 = c_3 = 0$ and $c_1 = 1$, for which $\gamma_{\min}/\gamma_{\max} = 1/2$. One can see that mild anisotropy has very little influence on the average step velocity. Put differently: V_{avg} is not sensitive to the actual Wulff shape, but rather to the degree of anisotropy or, equivalently, the ratio $\gamma_{\min}/\gamma_{\max}$.

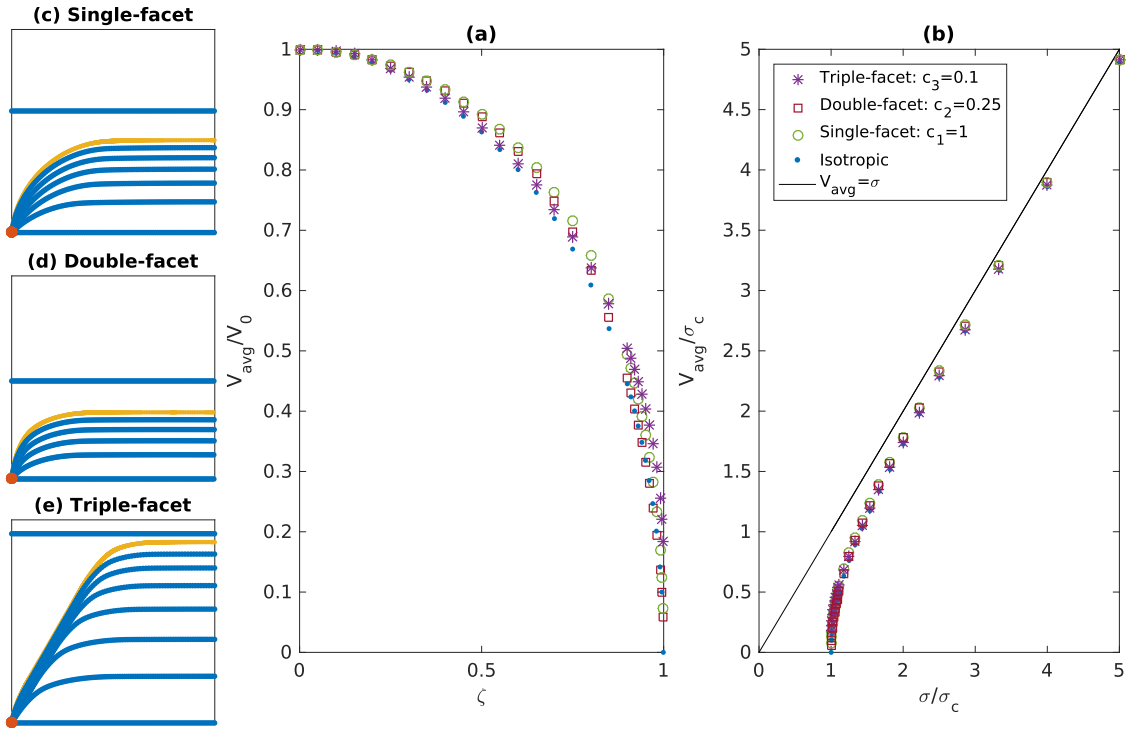


Figure 7: Average step velocity as function of (a) the percolation parameter $\zeta = \xi/\xi_c$ and (b) the supersaturation σ/σ_c for surface energies with a relatively low degree of anisotropy. The mobility is isotropic. Results of simulations are shown for four different cases: isotropic surface energy, single-facet motion ($c_1 \neq 0$), double-facet motion ($c_2 \neq 0$), and triple-facet motion ($c_3 \neq 0$). Panels (c)- (e) illustrate a series of fixed time front snapshots for $\zeta = 0.9$. The yellow curves denote the stationary front configurations, corresponding to $\zeta = 1$.

High anisotropy of surface energy

In some physical systems, the Wulff shape has a large aspect ratio corresponding to high anisotropy of the surface energy. To address such situations, the single-facet case was combined with the double- and triple-facet cases. The results are shown in Figure 8. One can see that the shape of the $V_{avg}(\zeta)$ curve is mostly controlled by the parameter c_1 or, roughly speaking, by the aspect ratio of the Wulff shape or by the ratio $\gamma_{min}/\gamma_{max}$. As the anisotropy increases ($c_1 \rightarrow \infty$), the average velocity approaches a step-like dependence on ζ : for large c_1 , V_{avg} stays approximately equal to V_0 for $\zeta < 1$ then drops sharply to 0 as ζ approaches 1. The corresponding behavior in terms of the supersaturation σ is that V_{avg} is approximately equal to σ for $\sigma > \sigma_c$, then drops sharply to 0 as σ decreases to σ_c .

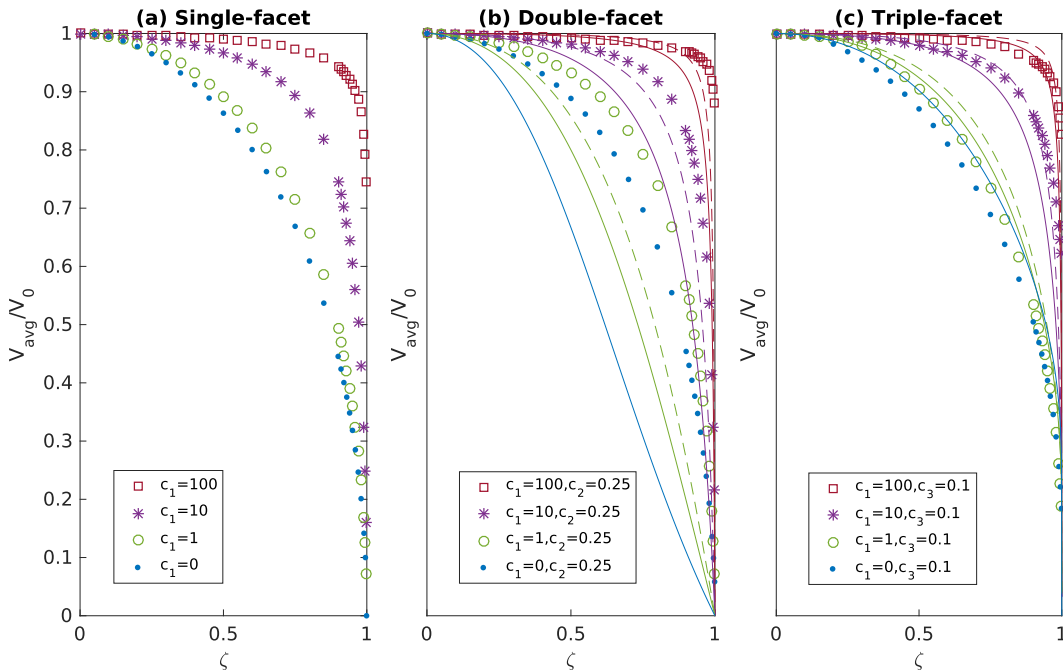


Figure 8: Average step velocity as a function of the percolation parameter for the (a) single-facet, (b) double-facet, and (c) triple-facet cases, including examples with a relatively high degree of anisotropy ($c_1 = 10$ and 100). The mobility is isotropic. Symbols indicate numerical data; solid and dashed lines show the analytical results for the corresponding fully-faceted models. In (b), the solid lines correspond to choosing α by Eq. (18) and the dashed lines correspond to choosing α by Eq. (19). In (c), the solid lines correspond to choosing α by Eq. (16) and the dashed lines correspond to choosing α by Eq. (17). Note that when $c_1 = 0$, the solid and dashed lines coincide.

Figure 8 contains a lot of information, so we dwell on it a bit. Parts (b) and (c) of the figure explore the idea that when γ is such that the interface is mostly faceted, the behavior can be approximated by considering a corresponding fully-faceted case (for which a closed-form solution is available). To implement this idea we must identify, for a given γ (whose Frank diagram is close to a convex polygon), a corresponding fully-faceted case. Focusing on our triple-faceted surface energies (i.e. on γ of the form (6) with $c_2 = 0$ and c_3 approaching $1/8$), there are two natural approaches to defining a correspondence. Both rely on the fact that the analytical solution of the fully-faceted case is determined by $\alpha = L_{cs}/L_{ch} = \gamma_h/(2\gamma_s - \gamma_h)$, where L_{cs} and L_{ch} are the critical lengths for the slanted and horizontal facets respectively, while γ_s and γ_h are the surface energies at the facet orientations. The first approach chooses α using the values of γ at the facets: when γ is given by Eq. (6) with $c_2 = 0$ it gives

$$\alpha = \frac{\gamma(0)}{2\gamma(\pi/3) - \gamma(0)} = \frac{1}{1 + \sqrt{3}c_1}. \quad (16)$$

The second approach chooses α using the values of L_{cs} and L_{ch} for the given γ , obtained using Eq. (9); this gives

$$\alpha = \frac{[\gamma'(\pi/3)]}{[\gamma'(0)]} = \frac{3c_3}{c_1 + 3c_3} = \frac{1}{1 + (c_1/3c_3)}. \quad (17)$$

Notice that while the two approaches differ in general, they both give $\alpha = 1$ when $c_1 = 0$. Figure 8(c) shows that when $c_3 = 0.1$, the exact solutions obtained using either (16) or (17) provide good approximations to the numerically-computed behavior of V_{avg} .

The value of our analytical solution to the fully-faceted case is not limited to the study of anisotropic surface energies. In fact, we showed in Figure 7 that the behavior of V_{avg} in the isotropic case is not much different from that of our numerical γ with $c_1 = c_2 = 0$ and $c_3 = 0.1$. Therefore our analytical solution for the symmetric fully-faceted case (where $\alpha = 1$ and the Wulff shape is a regular hexagon) provides an alternative to Potapenko's approximate

formula for V_{avg} , Eq. (2). Of course, neither our analytical formula nor Potapenko's formula is exact in the isotropic setting. But our analytical formula has the attractive feature of being exact for a particular (mildly anisotropic) surface energy.

We turn now to the double-faceted analogue of the preceding discussion. When γ has the form (6) with $c_3 = 0$ and c_2 near $1/3$, the Wulff shape resembles a rectangle, and it is natural to compare the numerical results with those of a fully-faceted model whose Wulff shape is exactly rectangular. There are, as before, two alternative ways to choose the fully-faceted model. Recall that in the double-faceted setting, the analytical solution of our fully-faceted model is determined by $\alpha = L_{cs}/L_{ch} = \gamma_h/\gamma_s$, where L_{cs} and L_{ch} are the critical lengths for the vertical and horizontal facets respectively, while γ_s and γ_h are the surface energies at the facet orientations. Choosing α using the values of γ at the facets gives the double-faceted analogue of Eq. (16):

$$\alpha = \frac{\gamma(0)}{\gamma(\pi/2)} = \frac{1}{1 + c_1}. \quad (18)$$

Choosing α using the the values of L_{cs} and L_{ch} for the given γ , obtained using Eq. (9), gives the double-faceted analogue of Eq. (17):

$$\alpha = \frac{[\gamma'(\pi/2)]}{[\gamma'(0)]} = \frac{4c_2}{2c_1 + 4c_2} = \frac{1}{1 + (c_1/2c_2)}. \quad (19)$$

The two choices are different in general, though they agree (giving $\alpha = 1$) when $c_1 = 0$.

Figure 8(b) compares our numerical results for some double-faceted surface energies to the behavior of the corresponding fully-faceted models. The numerical and analytical models do not agree very well in this case, and it is easy to understand why not. The disagreement reflects the quirk (noted earlier) of the double-facet case, whereby side facets are oriented perpendicular to the step propagation direction, i.e. they coincide with the orientation at which pinch-off should occur. In our numerical solutions, pinch-off occurs when the step orientation near the stopper deviates from vertical by a pinning angle threshold ϕ_c ; thus an exactly vertical orientation is never seen, and a vertical facet never forms. Our numerical

solution is the physically correct one, since pinch-off should happen as the step orientation approaches the vertical direction. The non-physical character of the exact solution for the double-facet case is a reminder that in some special cases, neglecting the curved segments that connect straight facets is not a good idea.

Non-constant mobility

We have thus far only considered the anisotropy of the surface energy; the mobility has been taken to be isotropic. However, the mobility is anisotropic for most crystals. Indeed, the anisotropy of the kinetic coefficient can be much higher than the anisotropy of the surface energy, due to the exponential dependence of the kinetic coefficient on the activation barrier for attachment of growth units. For example, the six $\langle 10\bar{1}0 \rangle$ steps on $\{0001\}$ faces of L-cystine show less than a two-fold difference in the surface energy but can exhibit a seven-fold difference in the kinetic coefficient.²⁴ Since both parameters are related to the bond strength, higher surface energy is associated with a higher kinetic coefficient and vice versa.

Here, we perform a limited analysis of mobility by contrasting constant mobility, $M(\theta) \equiv 1$, and anisotropic mobility, $M(\theta) = (1 + m|\sin(\theta)|)/(1 + m)$, for a step with anisotropic surface energy ($c_1 > 0$ and $c_2 = c_3 = 0$). Figure 9 reveals only a small effect of mobility superimposed on the effect of surface energy. Note that the unimpeded velocities, $V_0 = M(0)\sigma$, now depend on the mobility.

Conclusions

Macroscopic front-tracking simulations were performed to assess existing formulas for crystal growth inhibition by large immobile stoppers (the Cabrera-Vermilyea inhibition mechanism) and to examine what happens for anisotropic steps. Also, analytic solutions were obtained for some fully-faceted models, and their behavior was compared to that of the numerical simulations.

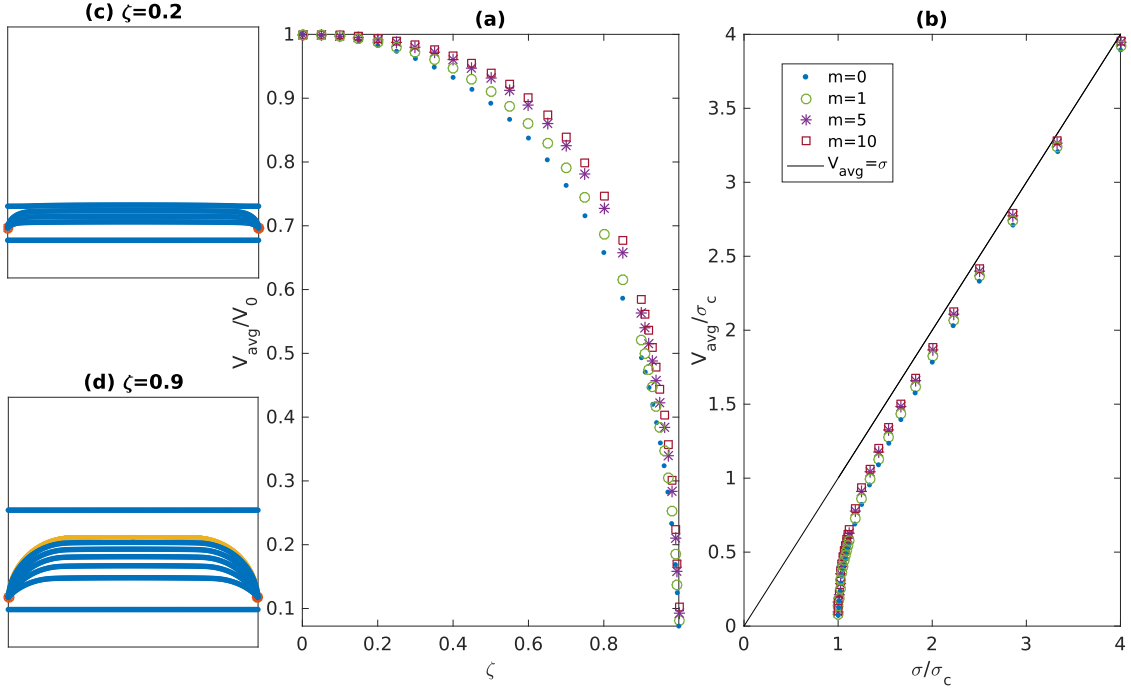


Figure 9: Average step velocity as a function of **(a)** the percolation parameter $\zeta = \xi/\xi_c$ and **(b)** the supersaturation σ/σ_c , for a fixed anisotropic single-facet surface energy ($c_1 = 1$, $c_2 = c_3 = 0$) and anisotropic single-facet mobility of the form $M(\theta) = (1+m|\sin(\theta)|)/(1+m)$, with $m \in \{0, 1, 5, 10\}$. Panels (c) and (d) give a series of fixed-time front snapshots for $\zeta = 0.2$ and $\zeta = 0.9$, respectively, for the case $m = 1$. The yellow curve in (d) shows the stationary front configuration, corresponding to $\zeta = 1$.

For an isotropic step (when the equilibrium Wulff shape of a corresponding 2D nucleus is a circle), the Potapenko model (Eq. (2)) was shown to provide a better description of step propagation through an array of large immobile stoppers compared to the classic C-V model (Eq. (1)). This is especially true near the percolation threshold, $\zeta \rightarrow 1$.

For steps with facets, if surface energy anisotropy is not very large (i.e. if the equilibrium Wulff shape approximates a polygon of moderate eccentricity), then the situation is not much different from the isotropic one: the dependence of $V_{avg}(\zeta)$ is only slightly steeper. In this case, the average velocity of the front is well approximated by Potapenko's formula, and also by the analytical result obtained using the fully-faceted model with a regular hexagon as its Wulff shape (Eq. (15) with $\alpha = 1$).

For steps with facets, as the surface energy anisotropy gets larger (i.e. when the aspect ratio of the approximately polygonal Wulff shape gets larger) the dependence of V_{avg} on the percolation parameter ζ becomes steeper. In the limit $\gamma_{min}/\gamma_{max} \rightarrow 0$, V_{avg} has almost step-like behavior: $V_{avg} \approx V_0$ for all ζ except as $\zeta \rightarrow 1$, where V_{avg} steeply drops to zero. Making the mobility (as well as the surface energy) anisotropic – with a kinetic coefficient proportional to the surface energy – does not change the behavior significantly.

We remind the reader that this analysis has been performed within the many assumptions embedded in the original C-V model. Some of these assumptions, such as high kink density on growth steps and large immobile stoppers, hold for certain systems, e.g. crystallization of ice in the presence of antifreeze proteins,^{27,52} potassium dihydrogen phosphate in the presence of Me^{3+} colloidal particles,¹⁰ or calcium oxalate monohydrate with acidic peptides.^{15–18} However, direct applicability of our plots and formulas is further limited by the assumption that all stoppers are distributed in a square-grid fashion; in real systems the distribution is typically random. For further progress, it will be important to consider how the results are affected by stochastic stopper distributions.

Acknowledgement

This work was supported primarily by the MRSEC Program of the National Science Foundation under Award Number DMR-1420073. RVK acknowledges additional support from NSF grant DMS-1311833.

Supporting Information Available

A Supplementary Information file, `crystal_growth_SI.pdf`, is available. It provides a detailed description of our numerical algorithm; information on the effect of our regularization; a derivation of our analytical formulas for the fully-faceted cases; and information on how the velocity of a facet depends on its length.

References

- (1) Jones, F.; Ogden, M. I. Controlling crystal growth with modifiers. CrystEngComm **2010**, 12, 1016–1023.
- (2) Lovette, M. A.; Browning, A. R.; Griffin, D. W.; Sizemore, J. P.; Snyder, R. C.; Doherty, M. F. Crystal shape engineering. Ind. Eng. Chem. Res. **2008**, 47, 9812–9833.
- (3) Sangwal, K. Additives and crystallization processes: from fundamentals to applications; John Wiley & Sons, 2007.
- (4) De Yoreo, J. J.; Vekilov, P. G. In Biom mineralization; Dove, P. M., De Yoreo, J. J., Weiner, S., Eds.; Mineralogical Society of America Geochemical Society: Washington, DC, USA, 2003; Vol. 54; pp 57–93.
- (5) Shtukenberg, A. G.; Lee, S. S.; Kahr, B.; Ward, M. D. Manipulating crystallization with molecular additives. Ann. Rev. Chem. Biomol. Eng. **2014**, 5, 77–96.

- (6) Qiu, S. R.; Orme, C. A. Dynamics of biomineral formation at the near-molecular level. Chem. Rev. **2008**, 108, 4784–4822.
- (7) Bliznakov, G. Sur le mécanisme de l'action des additifs adsorbants dans la croissance cristalline. Adsorption et croissance cristalline. Editions du Centre Nat. de la Recherche Sci. **1965**, 291–301.
- (8) Chernov, A. A. Modern crystallography III: Crystal growth; Springer, 1984; Vol. 36.
- (9) Cabrera, N.; Vermilyea, D. A. In Growth and perfection of crystals; Doremus, R., Roberts, B., Turnbull, D., Eds.; Wiley: New York: Cooperstown, NY, 1958; pp 393–410.
- (10) Rashkovich, L.; Kronskey, N. Influence of Fe^{3+} and Al^{3+} ions on the kinetics of steps on the {100} faces of KDP. J. Cryst. Growth **1997**, 182, 434–441.
- (11) Shekunov, B. Y.; Grant, D. J.; Latham, R. J.; Sherwood, J. N. In situ optical interferometric studies of the growth and dissolution behavior of paracetamol (acetaminophen) crystals. 3. Influence of growth in the presence of p-acetoxyacetanilide. J. Phys. Chem. B **1997**, 101, 9107–9112.
- (12) Ristić, R.; Shekunov, B. Y.; Sherwood, J. N. Growth of the tetrahedral faces of sodium chlorate crystals in the presence of dithionate impurity. J. Cryst. Growth **1994**, 139, 336–343.
- (13) Weaver, M. L.; Qiu, S. R.; Hoyer, J. R.; Casey, W. H.; Nancollas, G. H.; De Yoreo, J. J. Improved model for inhibition of pathological mineralization based on citrate–calcium oxalate monohydrate interaction. ChemPhysChem **2006**, 7, 2081–2084.
- (14) Weaver, M. L.; Qiu, S. R.; Hoyer, J. R.; Casey, W. H.; Nancollas, G. H.; De Yoreo, J. J. Inhibition of calcium oxalate monohydrate growth by citrate and the effect of the background electrolyte. J. Cryst. Growth **2007**, 306, 135–145.

- (15) Weaver, M. L.; Qiu, S. R.; Hoyer, J. R.; Casey, W. H.; Nancollas, G. H.; De Yoreo, J. J. Surface aggregation of urinary proteins and aspartic acid-rich peptides on the faces of calcium oxalate monohydrate investigated by in situ force microscopy. Calcif. Tissue Int. **2009**, 84, 462–473.
- (16) Weaver, M. L.; Qiu, S. R.; Friddle, R. W.; Casey, W. H.; De Yoreo, J. J. How the overlapping time scales for peptide binding and terrace exposure lead to nonlinear step dynamics during growth of calcium oxalate monohydrate. Cryst. Growth Des. **2010**, 10, 2954–2959.
- (17) Friddle, R. W.; Weaver, M. L.; Qiu, S. R.; Wierzbicki, A.; Casey, W. H.; De Yoreo, J. J. Subnanometer atomic force microscopy of peptide–mineral interactions links clustering and competition to acceleration and catastrophe. Proc. Natl. Acad. Sci. U. S. A. **2010**, 107, 11–15.
- (18) Cho, K. R.; Salter, E. A.; De Yoreo, J. J.; Wierzbicki, A.; Elhadj, S.; Huang, Y.; Qiu, S. R. Growth inhibition of calcium oxalate monohydrate crystal by linear aspartic acid enantiomers investigated by in situ atomic force microscopy. CrystEngComm **2013**, 15, 54–64.
- (19) Davis, K. J.; Dove, P. M.; De Yoreo, J. J. The role of Mg^{2+} as an impurity in calcite growth. Science **2000**, 290, 1134–1137.
- (20) Wasylenki, L. E.; Dove, P. M.; De Yoreo, J. J. Effects of temperature and transport conditions on calcite growth in the presence of Mg^{2+} : Implications for paleothermometry. Geochim. Cosmochim. Acta **2005**, 69, 4227–4236.
- (21) Wasylenki, L. E.; Dove, P. M.; Wilson, D. S.; De Yoreo, J. J. Nanoscale effects of strontium on calcite growth: An in situ AFM study in the absence of vital effects. Geochim. Cosmochim. Acta **2005**, 69, 3017–3027.

- (22) Van Driessche, A. E. S.; Sazaki, G.; Dai, G.; Otalora, F.; Gavira, J. A.; Matsui, T.; Yoshizaki, I.; Tsukamoto, K.; Nakajima, K. Direct observation of adsorption sites of protein impurities and their effects on step advancement of protein crystals. Cryst. Growth Des. **2009**, 9, 3062–3071.
- (23) Sleutel, M.; Van Driessche, A. E. S. On the self-purification cascade during crystal growth from solution. Cryst. Growth Des. **2013**, 13, 688–695.
- (24) Shtukenberg, A. G.; Poloni, L. N.; Zhu, Z.; An, Z.; Bhandari, M.; Song, P.; Rohl, A. L.; Kahr, B.; Ward, M. D. Dislocation-actuated growth and inhibition of hexagonal L-cystine crystallization at the molecular level. Cryst. Growth Des. **2015**, 15, 921–934.
- (25) Poloni, L. N.; Zhu, Z.; Garcia-Vázquez, N.; Yu, A. C.; Connors, D. M.; Hu, L.; Sahota, A.; Ward, M. D.; Shtukenberg, A. G. Role of molecular recognition in L-cystine crystal growth inhibition. Cryst. Growth Des. **2017**, 17, 2767–2781.
- (26) Sangwal, K. Kinetic effects of impurities on the growth of single crystals from solutions. J. Cryst. Growth **1999**, 203, 197–212.
- (27) Vorontsov, D. A.; Sazaki, G.; Hyon, S.-H.; Matsumura, K.; Furukawa, Y. Antifreeze effect of carboxylated ϵ -poly-L-lysine on the growth kinetics of ice crystals. J. Phys. Chem. B **2014**, 118, 10240–10249.
- (28) Miura, H.; Tsukamoto, K. Role of impurity on growth hysteresis and oscillatory growth of crystals. Cryst. Growth Des. **2013**, 13, 3588–3595.
- (29) Miura, H. Numerical study of impurity-induced growth hysteresis on a growing crystal surface. Cryst. Growth Des. **2016**, 16, 2033–2039.
- (30) Punin, Y. O.; Artamonova, O. I. Growth rate hysteresis of KH_2PO_4 crystals. Kristallografiya **1989**, 34, 1262–1266.

- (31) Kubota, N.; Yokota, M.; Doki, N.; Guzman, L. A.; Sasaki, S.; Mullin, J. W. A mathematical model for crystal growth rate hysteresis induced by impurity. Cryst. Growth Des. **2003**, 3, 397–402.
- (32) Kubota, N.; Mullin, J. W. A kinetic model for crystal growth from aqueous solution in the presence of impurity. J. Cryst. Growth **1995**, 152, 203–208.
- (33) Ristic, R. I.; DeYoreo, J. J.; Chew, C. M. Does impurity-induced step-bunching invalidate key assumptions of the Cabrera-Vermilyea model? Cryst. Growth Des. **2008**, 8, 1119–1122.
- (34) Land, T. A.; Martin, T. L.; Potapenko, S.; Palmore, G. T.; De Yoreo, J. J. Recovery of surfaces from impurity poisoning during crystal growth. Nature **1999**, 399, 442–445.
- (35) Potapenko, S. Y. Moving of step through impurity fence. J. Cryst. Growth **1993**, 133, 147–154.
- (36) van Enkevort, W. J. P.; Van den Berg, A. C. J. F. Impurity blocking of crystal growth: a Monte Carlo study. J. Cryst. Growth **1998**, 183, 441–455.
- (37) Lutsko, J. F.; González-Segredo, N.; Durán-Olivencia, M. A.; Maes, D.; Van Driessche, A. E. S.; Sleutel, M. Crystal growth cessation revisited: The physical basis of step pinning. Cryst. Growth Des. **2014**, 14, 6129–6134.
- (38) van Enkevort, W. J. P.; Los, J. H. “Tailor-made” inhibitors in crystal growth: A Monte Carlo simulation study. J. Phys. Chem. C **2008**, 112, 6380–6389.
- (39) Sleutel, M.; Lutsko, J. F.; Maes, D.; Van Driessche, A. E. S. Mesoscopic Impurities Expose a Nucleation-Limited Regime of Crystal Growth. Phys. Rev. Lett. **2015**, 114, 245501.
- (40) De Yoreo, J. J.; Zepeda-Ruiz, L. A.; Friddle, R. W.; Qiu, S. R.; Wasylenki, L. E.; Chernov, A. A.; Gilmer, G. H.; Dove, P. M. Rethinking classical crystal growth models

- through molecular scale insights: Consequences of kink-limited kinetics. Cryst. Growth Des. **2009**, 9, 5135–5144.
- (41) Kupier, M.; Morton, C.; Abraham, S.; Gray-Weale, A. The biological function of an insect antifreeze protein simulated by molecular dynamics. eLife **2015**, 4, e05142.
- (42) Miura, H. Phase-field modeling of step dynamics on growing crystal surface: step pinning induced by impurities. Cryst. Growth Des. **2015**, 15, 4142–4148.
- (43) Teng, H. H.; Dove, P. M.; Orme, C. A.; De Yoreo, J. J. Thermodynamics of calcite growth: Baseline for understanding biomineral formation. Science **1998**, 282, 724–727.
- (44) Rashkovich, L. N.; Petrova, E. V.; Shustin, O. A.; Chernevich, T. G. Formation of a dislocation spiral on the (010) face of a potassium hydrogen phthalate crystal. Phys. Solid State **2003**, 45, 400–407.
- (45) Chernov, A. A. Notes on interface growth kinetics 50 years after Burton, Cabrera and Frank. J. Cryst. Growth **2004**, 264, 499–518.
- (46) Rashkovich, L. N.; De Yoreo, J. J.; Orme, C. A.; Chernov, A. A. In situ atomic force microscopy of layer-by-layer crystal growth and key growth concepts. Crystallogr. Rep. **2006**, 51, 1063–1074.
- (47) Oberman, A.; Osher, S.; Takei, R.; Tsai, R. Numerical methods for anisotropic mean curvature flow based on a discrete time variational formulation. Commun. Math. Sci **2011**, 9, 637–662.
- (48) Miura, H.; Kobayashi, R. Phase-field modeling of step dynamics on growing crystal surface: Direct integration of growth units to step front. Cryst. Growth Des. **2015**, 15, 2165–2175.
- (49) Kobayashi, R.; Giga, Y. On anisotropy and curvature effects for growing crystals. Japan J. Indust. Appl. Math. **2001**, 18, 207–230.

- (50) Taylor, J. E. II – mean curvature and weighted mean curvature. Acta Metallurgica et Materialia **1992**, 40, 1475–1485.
- (51) Angenent, S.; Gurtin, M. E. Multiphase thermomechanics with interfacial structure 2. Evolution of an isothermal interface. Archive for Rational Mechanics and Analysis **1989**, 108, 323–391.
- (52) Kubota, N. Effects of cooling rate, annealing time and biological antifreeze concentration on thermal hysteresis reading. Cryobiology **2011**, 63, 198–209.

For Table of Contents Use Only

Effect of step anisotropy on crystal growth inhibition by immobile impurity stoppers

James P. Lee-Thorp, Alexander G. Shtukenberg, and Robert V. Kohn

Synopsis: Step pinning by adsorbed impurities is an important crystal growth inhibition mechanism. A seminal 1958 study by Cabrera and Vermilyea considered a periodic array of pinning sites. We revisit this problem using numerical simulations and a new type of analytical approximation, for anisotropic surface energies that induce faceting. The average step velocity is surprisingly insensitive to anisotropy.

